Nonlinear Robust Safety Factor Profile Control in Tokamaks via Feedback Linearization and Nonlinear Damping Techniques

Andres Pajares and Eugenio Schuster

***Abstract*— Tokamaks are toroidal devices in which a plasma is confined by means of helical magnetic fields with the purpose of obtaining energy from nuclear fusion reactions. The safety factor, q, is a magnitude that measures the pitch of the helical magnetic field lines in a tokamak. Active control of the q profile is needed due to its close relationship with plasma performance (steady-state operation) and magneto-hydrodynamic stability. However, the responses of some plasma magnitudes, such as the electron temperature profile, are difficult to model and introduce a high level of uncertainty in the model used for q-profile control design. Control algorithms that are robust against such model uncertainties must be developed in order to ensure successful q-profile regulation. In this work, a nonlinear, robust q-profile controller is designed using feedback linearization and nonlinear damping techniques. The controller makes use of plasma current modulation, neutral beam injection, electron-cyclotron heating & current drive, and electron density modulation as actuation methods. A simulation study is carried out for a DIII-D scenario to test the controller's performance under the presence of electron temperature uncertainties.**

I. Introduction

A plasma is a very hot gas in which ions and electrons are dissociated. Such dissociation makes plasmas capable of interacting with magnetic fields, as well as of driving electrical current. These special characteristics of plasmas gave birth, within the context of nuclear fusion research, to the so-called tokamak [1]. Tokamaks are toroidal devices in which a plasma is confined by means of helical magnetic fields (see Fig. 1). The ultimate goal of tokamaks is to obtain energy by means of nuclear fusion reactions within the plasma, which must be heated to temperatures in the order of 10 million degrees to overcome the Coulombic repulsion force that exists between its particles (usually hydrogen isotopes) and achieve fusion. The pitch of the helical magnetic field lines within the tokamak can be characterized by a magnitude known as safety factor, q. This magnitude is closely related to steady-state operation, as well as to certain plasma magneto-hydrodynamic (MHD) instabilities [1] that normally decrease performance. Therefore, active control of the q profile is a requirement for tokamaks to become a commercially competitive means of energy generation.

Significant research has been carried out to develop q-profile controllers for tokamaks. Control of the q profile was experimentally demonstrated in both low and high plasma-confinement scenarios in the DIII-D tokamak [2], [3], [4], [5]. Other previous work proposed q-profile controllers for other tokamaks such as NSTX-U [6], JET [7], Tore Supra [8], TCV [9], or ITER [10], the next-generation tokamak currently under construction.

A relevant aspect of this control problem is that there is always some degree of uncertainty when modeling the response of the q profile to the different actuators. In particular, it is extremely difficult to accurately capture the dynamics of kinetic magnitudes such as the plasma temperature by using models that are tractable for control design. Most of our previous model-based control-design work employs a control-oriented model [11] for the electron temperature evolution that exploits the time-scale separation between kinetic (e.g., temperature) and magnetic (e.g., q) variables. Whereas this modeling approach has the advantage of substantially facilitating the control design, the capability of the simplified temperature model to accurately capture the real dynamics is limited, which may result in poor controller performance. Alternatively, a more complex temperature model based on the electron heat-transport equation is used in other pieces of our previous work [9]. However, the low-complexity transport-coefficients models that are needed for control design still introduce a high level of uncertainty that can affect controller performance. Therefore, robust controllers that ensure successful q-profile regulation even in the presence of the aforementioned uncertainties are required.

Controllers that are robust to electron temperature uncertainties were proposed in [9], [10], [12], where approximate linearization and linear robust techniques are employed. In this work, a nonlinear, robust q-profile controller that avoids approximate linearization is designed to handle model uncertainties in the model used for the electron temperature profile evolution. A nominal controller is first designed by using feedback linearization techniques based on a model without uncertainties, in a similar fashion as in [13]. As a difference from previous work, electron density modulation is included as an actuator, together with plasma current modulation, neutral-beam injection (NBI), and electron-cyclotron (EC) heating & current drive. More importantly, nonlinear damping techniques are used in this work to robustify the nominal design and to therefore avoid performance limitation arising from the feedback linearization method due to the temperature-profile-evolution model uncertainties.

This work is organized as follows. The nonlinear model for the q-profile evolution is described in Section II. The nominal control law is presented in Section III. The robust control law is designed in Section IV. A simulation study is presented in Section V to test the controller performance. Finally, some conclusions are presented in Section VI.

This work was supported in part by the U.S. Department of Energy (DE-SC0010661). A. Pajares (andres.pajares@lehigh.edu) and E. Schuster are with the Department of Mechanical Engineering and Mechanics, Lehigh University, Bethlehem, PA 18015, USA.

Preprint submitted to 2018 IEEE Conference on Control Technology and Applications. Received February 1, 2018.

II. Safety Factor Evolution Model

Magnetic field lines guide the particles in helical, closed paths in tokamaks (see Fig. 1). This helical magnetic field, $\bar{B}$, has two components, namely the toroidal magnetic field, $\bar{B}_\phi$, and the poloidal magnetic field, $\bar{B}_\theta$, such that $\bar{B} = \bar{B}_\phi + \bar{B}_\theta$. The poloidal magnetic flux at a point P is defined as $\Psi = \int_S \bar{B}_\theta \cdot d\bar{S}$, where S is the surface whose boundary is a toroidal ring passing through P and is normal to the z-axis (see Fig. 1). Points with the same poloidal magnetic flux, Ψ, define nested magnetic-flux surfaces. Under ideal MHD conditions, an axisymmetric configuration around the z-axis is normally found in tokamaks (see Fig. 2). This, together with the fact that some key plasma properties are constant on the magnetic-flux surfaces, allows for the use of a one-dimensional model in the spatial domain when the mean effective minor radius, ρ, indexing the magnetic-flux surfaces, is used as spatial coordinate. This spatial coordinate is normalized as $\hat{\rho} = \rho/\rho_b$, where ρ_b is the value of ρ at the last closed magnetic-flux surface (see Fig. 2). The normalized mean effective minor radius, $\hat{\rho}$, is related to the toroidal magnetic flux, Φ, and to the vacuum toroidal magnetic field at the geometric major radius R_0 of the tokamak, $B_{\phi,0}$, by means of $\pi B_{\phi,0}\rho_b^2\hat{\rho}^2 = \Phi$. The q profile is defined as

$$q(\hat{\rho},t) \triangleq \frac{d\Phi}{d\Psi} = -\frac{d\Phi}{2\pi d\psi} = -\frac{B_{\phi,0}\rho_b^2\hat{\rho}}{\partial\psi/\partial\hat{\rho}}, \tag{1}$$

where t is the time and $\psi(\hat{\rho},t)$ is the poloidal stream function, which satisfies $\Psi = 2\pi\psi$.

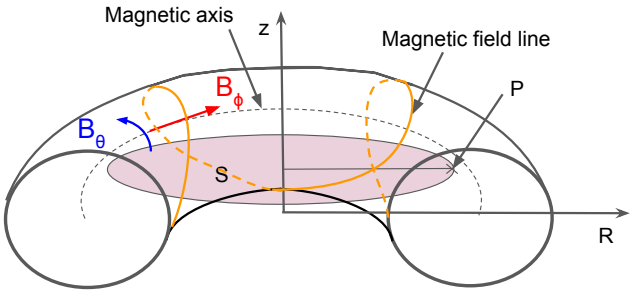

Fig. 1. Helical magnetic field lines in the tokamak define a poloidal magnetic flux through the surface S associated with the point P.

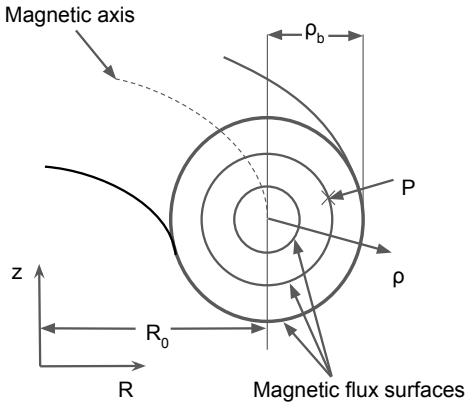

Fig. 2. Magnetic flux surfaces in a tokamak. Each magnetic flux surface is characterized by a constant poloidal magnetic flux Ψ.

The evolution of ψ is given by the magnetic diffusion equation [14],

$$\frac{\partial\psi}{\partial t} = \frac{\eta(T_e)}{\mu_0\rho_b^2\hat{F}^2}\frac{1}{\hat{\rho}}\frac{\partial}{\partial\hat{\rho}}\left(\hat{\rho}D_\psi\frac{\partial\psi}{\partial\hat{\rho}}\right) + R_0\hat{H}\eta(T_e)j_{ni}, \tag{2}$$

where $\eta(T_e)$ is the plasma resistivity, $T_e(\hat{\rho},t)$ is the electron temperature, μ_0 is the vacuum permeability, $D_\psi(\hat{\rho}) = \hat{F}(\hat{\rho})\hat{G}(\hat{\rho})\hat{H}(\hat{\rho})$, where $\hat{F}$, $\hat{G}$, and $\hat{H}$ are spatially varying geometric factors pertaining to the magnetic configuration of a particular plasma equilibrium [15], and $j_{ni}(\hat{\rho},t)$ is the non-inductive current density. The boundary conditions are given by

$$\left.\frac{\partial\psi}{\partial\hat{\rho}}\right|_{\hat{\rho}=0} = 0, \quad \left.\frac{\partial\psi}{\partial\hat{\rho}}\right|_{\hat{\rho}=1} = -\frac{\mu_0}{2\pi}\frac{R_0}{\hat{G}|_{\hat{\rho}=1}\hat{H}|_{\hat{\rho}=1}}I_p(t), \tag{3}$$

where $I_p(t)$ is the total plasma current.

In this work, $T_e(\hat{\rho},t)$ is considered to be an uncertain variable,

$$T_e(\hat{\rho},t) = T_e^{nom}(\hat{\rho},t) + \delta_{T_e}(\hat{\rho},t), \tag{4}$$

where $T_e^{nom}(\hat{\rho},t)$ is the nominal electron temperature obtained from control-oriented models [11], and $\delta_{T_e}(\hat{\rho},t)$ is an uncertain term that is unknown but it is assumed to be bounded. In this work, η and j_{ni} are modeled as in [11], so they are functions of T_e and, therefore, they are uncertain variables as well. They can be expressed as

$$\eta(\hat{\rho},t) = \eta^{nom}(\hat{\rho},t) + \delta_\eta(\hat{\rho},t), \tag{5}$$

$$j_{ni}(\hat{\rho},t) = j_{ni}^{nom}(\hat{\rho},t) + \delta_{j_{ni}}(\hat{\rho},t), \tag{6}$$

where $\eta^{nom}(\hat{\rho},t)$ and $j_{ni}^{nom}(\hat{\rho},t)$ are the nominal plasma resistivity and non-inductive current density, respectively, and $\delta_\eta(\hat{\rho},t)$ and $\delta_{j_{ni}}(\hat{\rho},t)$ are uncertain terms that are also unknown but bounded, and depend on $\delta_{T_e}(\hat{\rho},t)$. Using (5) and (6), equation (2) can be rewritten as

$$\frac{\partial\psi}{\partial t} = \frac{\eta^{nom}}{\mu_0\rho_b^2\hat{F}^2}\frac{1}{\hat{\rho}}\frac{\partial}{\partial\hat{\rho}}\left(\hat{\rho}D_\psi\frac{\partial\psi}{\partial\hat{\rho}}\right) + R_0\hat{H}\eta^{nom}j_{ni}^{nom} + \delta_\psi, \tag{7}$$

where δ_ψ is an uncertain term that is bounded and given by

$$\delta_\psi = \frac{\delta_\eta}{\mu_0\rho_b^2\hat{F}^2}\frac{1}{\hat{\rho}}\frac{\partial}{\partial\hat{\rho}}\left(\hat{\rho}D_\psi\frac{\partial\psi}{\partial\hat{\rho}}\right) + R_0\hat{H}(\delta_\eta\delta_{j_{ni}} + \delta_\eta j_{ni}^{nom} + \eta^{nom}\delta_{j_{ni}}).$$

It is convenient to define the poloidal flux gradient, θ, as

$$\theta \triangleq \frac{\partial\psi}{\partial\hat{\rho}}. \tag{8}$$

Taking derivative with respect to $\hat{\rho}$, using the definition (8), and applying the chain rule, equation (7) can be rewritten as

$$\frac{\partial\theta}{\partial t} = \left[h_{diff,1}(\hat{\rho})\theta'' + h_{diff,2}(\hat{\rho})\theta' + h_{diff,3}(\hat{\rho})\theta\right]u_\eta(t) + \sum_{i=1}^{N_{NB}} h_{NB,i}(\hat{\rho})u_{NB,i}(t) + h_{EC}(\hat{\rho})u_{EC}(t) + \left[h_{BS,1}(\hat{\rho})\frac{1}{\theta} - h_{BS,2}(\hat{\rho})\frac{\theta'}{\theta^2}\right]u_{BS}(t) + \delta_\theta, \tag{9}$$

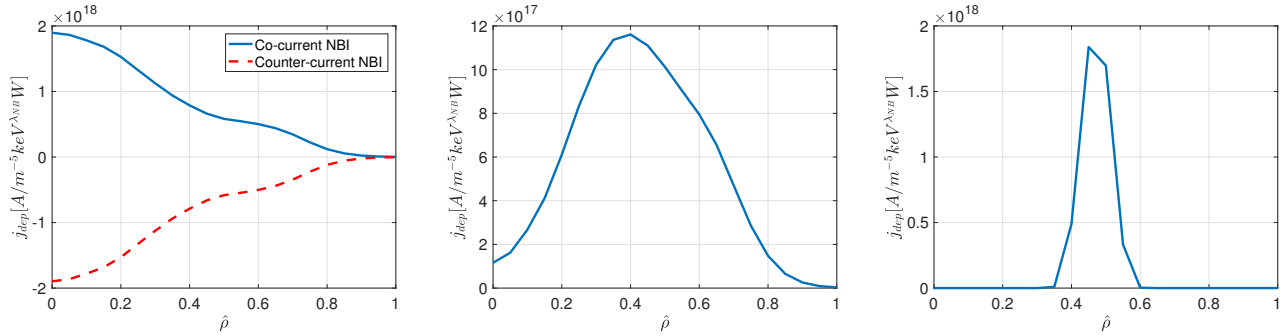

(a) On-axis NBI (b) Off-axis NBI (c) EC

Fig. 3. Current deposition profiles tailored to DIII-D shot 147634: (a) On-axis NBI, (b) Off-axis NBI, (c) EC.

where control-oriented models for T_e^{nom}, η^{nom}, and j_{ni}^{nom} have been employed [11]. N_{NB} is the number of NBI groups available for feedback-linearization control within the tokamak (see Section III-B for details), $h_{diff,(\cdot)}(\hat{\rho})$, $h_{NB,i}(\hat{\rho})$, $h_{EC}(\hat{\rho})$ and $h_{BS,(\cdot)}(\hat{\rho})$ are spatial functions whose expressions can be found in [13], $\delta_\theta \triangleq \delta'_\psi$, which is also assumed to be bounded, and $(\cdot)' \triangleq \partial(\cdot)/\partial\hat{\rho}$. The variables $u_\eta(t)$, $u_{NB,i}(t)$, $u_{EC}(t)$ and $u_{BS}(t)$ denote the virtual inputs to the system, which are functions of the physical inputs, i.e.,

$$u_\eta = I_p^{-3\gamma/2} P_{tot}^{-3\epsilon/2} \bar{n}_e^{-3\zeta/2}, \tag{10}$$

$$u_{NB,i} = I_p^{\gamma(\lambda_{NB}-\frac{3}{2})} P_{tot}^{\epsilon(\lambda_{NB}-\frac{3}{2})} \bar{n}_e^{\zeta(\lambda_{NB}-\frac{3}{2})-1} P_{NB,i}, \tag{11}$$

$$u_{EC} = I_p^{\gamma(\lambda_{EC}-\frac{3}{2})} P_{tot}^{\epsilon(\lambda_{EC}-\frac{3}{2})} \bar{n}_e^{\zeta(\lambda_{EC}-\frac{3}{2})-1} P_{EC}, \tag{12}$$

$$u_{BS} = I_p^{-\gamma/2} P_{tot}^{-\epsilon/2} \bar{n}_e^{1-\zeta/2}, \tag{13}$$

where $P_{NB,i}(t)$ is the power of the i-th NBI group ($i = 1, \ldots, N_{NB}$), $P_{EC}(t)$ is the EC power, $P_{tot}(t) = \sum_{i=1}^{N_{NB}} P_{NB,i}(t) + P_{EC}(t)$ is the total power injected, $\bar{n}_e(t)$ is the line-average electron density, γ, ϵ, ζ, λ_{NB} and λ_{EC} are constants arising from the T_e^{nom} and j_{ni}^{nom} control-oriented models [11]. The physical inputs I_p, $P_{NB,i}$, P_{EC} and $\bar{n}_e$ are considered to be the controllable inputs in this work. Finally, the boundary conditions can be rewritten as

$$\theta|_{\hat{\rho}=0} = 0, \quad \theta|_{\hat{\rho}=1} = -k_{I_p} I_p(t), \tag{14}$$

where $k_{I_p} = \mu_0 R_0 / (2\pi \hat{G}|_{\hat{\rho}=1} \hat{H}|_{\hat{\rho}=1})$.

III. Nominal Control Law

A. Discretization Using Finite Differences

The partial differential equation (9) is discretized in the $\hat{\rho}$-domain by means of the finite differences method for the nominal case (no uncertainty, $\delta_\theta = 0$). A grid with $N+1$ nodes in $\hat{\rho} = [0, 1]$ is used. The value of θ at each node is denoted by θ_j, for $j = 0, 1, ..., N$. After spatially discretizing (9), and using the boundary conditions (14), the model can be rewritten as

$$\dot{\hat{\theta}} = G\big(\hat{\theta}, I_p(t)\big) u(t), \tag{15}$$

$$\theta_N = -k_{I_p} I_p(t), \tag{16}$$

where $\dot{(\cdot)} \triangleq d(\cdot)/dt$, $\hat{\theta} = [\theta_1, ..., \theta_{N-1}]^T$ is a vector that only includes the values of θ at the inner nodes, $G\big(\hat{\theta}, I_p(t)\big) \in \mathbb{R}^{(N-1)\times(N_{NB}+3)}$, and $u(t) = [u_\eta(t), u_{NB,1}(t), ..., u_{NB,N_{NB}}(t), u_{EC}(t), u_{BS}(t)]^T$.

B. Determination of N_{NB}

The number of NBI groups available for feedback linearization control is determined based on the requirement of having N_{NB} linearly independent columns in G associated with $u_{NB,i}$ ($i = 1, ..., N_{NB}$). Such columns must also produce a well-conditioned subpart in G. These requirements attend to both physical reasons (the number of linearly independent columns represents the real number of nodes that can be controlled with NBI power modulation) and numerical reasons (feedback linearization requires a full rank, well-conditioned G matrix [13]).

Linear independence of the G-columns associated with $u_{NB,i}$ depends exclusively on the linear independence of the current deposition profiles (denoted by $j_{aux,i}^{prof}(\hat{\rho})$ in [13], notation that is kept in this work) associated with $u_{NB,i}$. This fact can be inferred from the definition of $h_{NB,i}(\hat{\rho})$, which can be obtained from [13]. Typical DIII-D current deposition profiles for on-axis NBI, off-axis NBI, and EC are depicted in Fig. 3 [11]. Although these particular $j_{aux,i}^{prof}(\hat{\rho})$ are tailored to a specific DIII-D shot, any other shot or tokamak would produce similar qualitative results regarding on-axis NBI, off-axis NBI, and EC current deposition profiles. It can be appreciated that for on-axis NBI, co-current NBI's and counter-current NBI's produce linearly dependent columns. Therefore, all on-axis NBI's are taken as one group. The power associated with this group is denoted by $P_{NB,ON-axis}$. Off-axis NBI's will be used as a single group because they produce a linearly independent column, and the power associated with this group is denoted by $P_{NB,OFF-axis}$. Then, two NBI groups are available for feedback linearization control: on-axis NBI and off-axis NBI ($N_{NB} = 2$). Finally, it can also be seen that EC produces a linearly independent column, due to its sharp off-axis current-deposition profile.

C. Determination of the Number of Nodes, $N+1$

The number of nodes in which the system is discretized is chosen equal to the number of physical inputs available for control. Due to the boundary condition (14), θ_0 is already fixed. θ at the other N nodes are to be controlled with the $N_{NB} + 3 = 5$ available physical inputs, thus $N = 5$. Therefore, in this work, $G \in \mathbb{R}^{4\times 5}$.

Preprint submitted to 2018 IEEE Conference on Control Technology and Applications. Received February 1, 2018.

Using the same nodes as available physical inputs only makes sense if the resulting matrix G is full row rank, which would imply that all nodes in the discretization can be controlled through the available physical inputs. For the practical cases studied in this work and in [13], it is found that G is full row rank. However, in general, it cannot be assured that G is full row rank. This is due to the nature of the system, as G depends on $\hat{\theta}$ and I_p. If G is not full rank, a study of the relative degree of the system needs to be carried out, and a change of variables $z = T(\hat{\theta})$ needs to be sought to find a state-space representation that is feedback linearizable [16]. Due to the nature of the auxiliary sources, however, it can always be assured that at least 3 inner nodes can be controlled (because G has at least 3 linearly independent columns arising from on-axis NBI, off-axis NBI and EC contributions), and that the system is always feedback linearizable with the new state variables $z = T(\hat{\theta})$.

D. Boundary Control with I_p

From the boundary condition (16), it can be seen that I_p directly controls θ_N. Then, the control law for I_p is taken as

$$I_p(t) = -\bar{\theta}_N / k_{I_p}, \tag{17}$$

where $\bar{\theta}_N$ is the target for θ_N. The control law (17) assures that $\theta_N = \bar{\theta}_N$ at all times. In this work, no model uncertainty is considered in (16) since determination of k_{I_p} is relatively accurate.

E. Interior Control: Feedback Linearization Control Law

If $u(t)$ is chosen such that

$$G(\hat{\theta}, I_p)u(t) = -k_N\tilde{\theta} + \dot{\bar{\theta}}, \tag{18}$$

where $k_N > 0$ is a design parameter, $\bar{\theta} = [\bar{\theta}_1, ..., \bar{\theta}_{N-1}]^T$ is a vector with the target values for $\hat{\theta}$, and $\tilde{\theta} = \hat{\theta} - \bar{\theta}$, then equation (15) can be rewritten as

$$\dot{\tilde{\theta}} = -k_N\tilde{\theta}, \tag{19}$$

i.e., a linear system which is exponentially stable because $k_N > 0$ [16]. A suitable Lyapunov function for (19) is given by $V = \frac{1}{2}\tilde{\theta}^T\tilde{\theta}$, which yields $\dot{V} = -k_N \sum_{i=1}^{i=N-1} \tilde{\theta}_i^2$. Hence, it can be assured that $\tilde{\theta} \to 0$ in time, or what is the same, that $\theta \to \bar{\theta}$ in time.

Expression (18) is a nonlinear system of 4 equations with 4 unknowns (u is a function of $P_{NB,ON-axis}$, $P_{NB,OFF-axis}$, P_{EC}, and $\bar{n}_e$, as given in equations (10)-(13)), whose solution defines the control law for these 4 physical inputs. At every control step, (18) is solved using a trust-region dogleg algorithm, which is based on solving an optimization problem [17]. Once a solution has been found, physical actuation limits for $P_{NB,ON-axis}$, $P_{NB,OFF-axis}$, P_{EC}, and $\bar{n}_e$ are applied. As long as such actuation limits are not reached, exponential stability of the $\tilde{\theta}$ evolution is ensured.

IV. Robust Control Law

A. Discretization Using Finite Differences

The partial differential equation (9) is also discretized in the $\hat{\rho}$-domain by means of the finite differences method for the case with uncertainty, $\delta_\theta \neq 0$. Using the same grid and notation as above, (9) can be rewritten as

$$\dot{\hat{\theta}} = G\big(\hat{\theta}, I_p(t)\big)u(t) + \hat{\delta}_\theta, \tag{20}$$

where $\hat{\delta}_\theta = [\delta_{\theta,1}, ..., \delta_{\theta,N-1}]^T$, being $\delta_{\theta,(\cdot)}$ the values of δ_θ at the discretization nodes. If $G\big(\hat{\theta}, I_p(t)\big)$ is full row rank (as in this case), it has a right inverse, which is denoted as $G_R^{-1}\big(\hat{\theta}, I_p(t)\big)$. Then, equation (20) can be rewritten as

$$\dot{\hat{\theta}} = G\big(\hat{\theta}, I_p(t)\big)\big[u(t) + G_R^{-1}\big(\hat{\theta}, I_p(t)\big)\hat{\delta}_\theta\big]. \tag{21}$$

Because δ_θ is bounded, it can be noted that $||\hat{\delta}_\theta||_2$ is bounded as well. Such bound, although unknown, is denoted by κ in this work ($\kappa > 0$).

B. Nonlinear Damping Control Law

A robust control law is sought using nonlinear damping techniques [16] with a shape given by

$$u(t) = u_n(t) + v(t), \tag{22}$$

where $u_n(t)$ is the nominal control law for the virtual inputs that is obtained from (18), and $v(t)$ is the nonlinear damping term that is designed for robustness. Using the Lyapunov function $V = \frac{1}{2}\tilde{\theta}^T\tilde{\theta}$, it is found that

$$\begin{aligned}\dot{V} &= \frac{\partial V}{\partial \tilde{\theta}}\Big(G\big[u_n + v + G_R^{-1}\hat{\delta}_\theta\big] - \dot{\bar{\theta}}\Big) \\ &= -k_N\tilde{\theta}^T\tilde{\theta} + \tilde{\theta}^T G\big[v + G_R^{-1}\hat{\delta}_\theta\big].\end{aligned} \tag{23}$$

By defining $w^T = \tilde{\theta}^T G$, and taking 2-norm, the second term on the right hand side of equation (23) can be bounded as

$$w^T\big[v + G_R^{-1}\hat{\delta}_\theta\big] \leq w^T v + ||w||_2||G_R^{-1}||_2\kappa, \tag{24}$$

and if v is taken as

$$v = -w||G_R^{-1}||_2^2 k_R, \tag{25}$$

where $k_R > 0$ is a design parameter, then (24) becomes

$$w^T\big[v + G_R^{-1}\hat{\delta}_\theta\big] \leq -||w||_2^2||G_R^{-1}||_2^2 k_R + ||w||_2||G_R^{-1}||_2\kappa. \tag{26}$$

Defining $x \triangleq ||w||_2||G_R^{-1}||_2$, it is trivial to see that $f(x) = -k_R x^2 + \kappa x$ has a maximum at $x_0 = \kappa/(2k_R)$, and $f(x_0) = \kappa^2/(4k_R^2)$. Therefore, equation (23) can be rewritten as

$$\dot{V} \leq -k_N||\tilde{\theta}||_2^2 + \frac{\kappa^2}{4k_R^2}, \tag{27}$$

so it is found that $\dot{V} < 0$ outside the ball B defined by $B = \{\tilde{\theta} \mid ||\tilde{\theta}||_2 < \frac{\kappa}{2k_R\sqrt{k_N}}\}$. Hence, $\tilde{\theta}$ is uniformly bounded in closed-loop under the robust control law (22), where v is given by (25).

Finally, the physical inputs to the system, $P_{NB,ON-axis}$, $P_{NB,OFF-axis}$, P_{EC}, and $\bar{n}_e$, are obtained from solving the nonlinear system of 4 equations given by

$$Gu = G(u_n - w||G_R^{-1}||_2^2 k_R), \tag{28}$$

Preprint submitted to 2018 IEEE Conference on Control Technology and Applications. Received February 1, 2018.

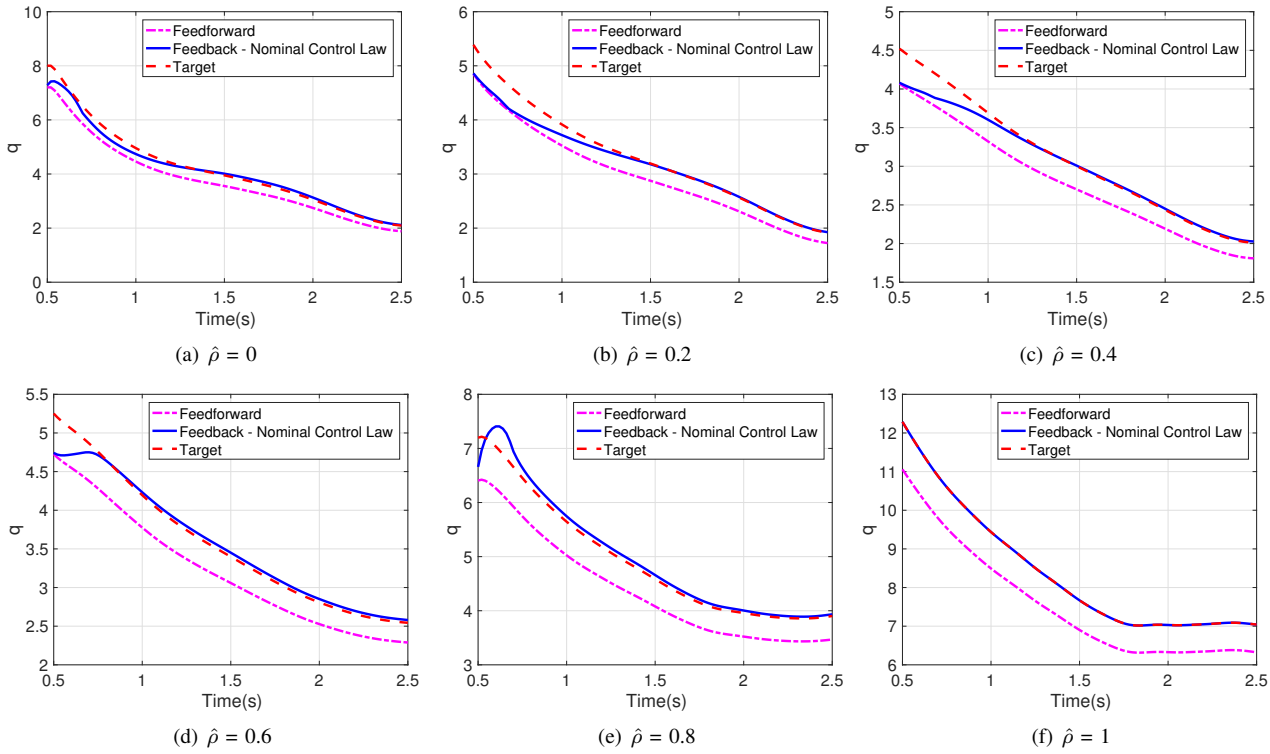

(a) $\hat{\rho}$ = 0 (b) $\hat{\rho}$ = 0.2 (c) $\hat{\rho}$ = 0.4

(d) $\hat{\rho}$ = 0.6 (e) $\hat{\rho}$ = 0.8 (f) $\hat{\rho}$ = 1

Fig. 4. Safety factor evolution at different locations for simulation case 1 ($\delta_{T_e} = 0$).

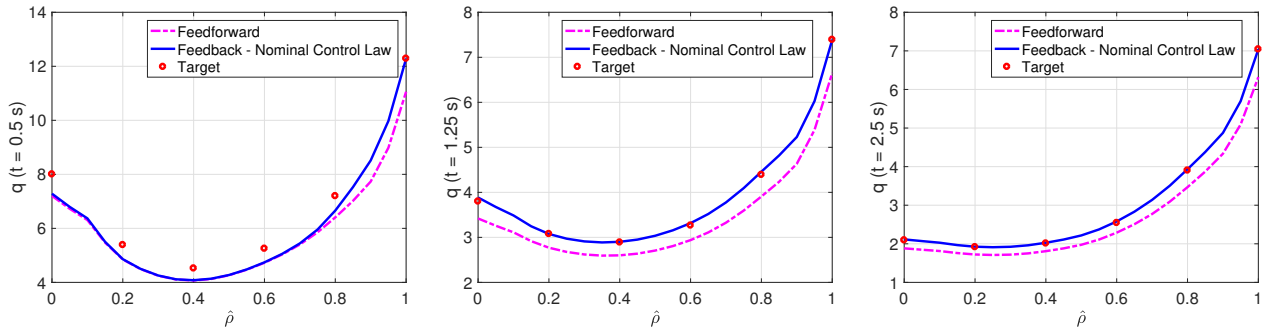

(a) t = 0.50 s (b) t = 1.25 s (c) t = 2.00 s

Fig. 5. Safety factor profiles for simulation case 1 ($\delta_{T_e} = 0$).

where u is, as indicated above, a function of $P_{NB,ON-axis}$, $P_{NB,OFF-axis}$, P_{EC}, and $\bar{n}_e$ as given by (10)-(13). As in the nominal case, a trust-region dogleg algorithm is used to solve (28), and subsequently physical actuation limits are applied. As long as these actuation limits are not reached, uniform boundedness of the $\tilde{\theta}$ evolution is ensured.

V. Simulation Study

In this section, a simulation study is carried out to show the performance of both nominal and robust control laws. The model is tailored to DIII-D shot 147634. The corresponding machine parameters are $B_{\phi,0}$ = 1.65 T, R_0 = 1.80 m, ρ_b = 0.82 m, γ = 1, ϵ = 0.5, ζ = -1, λ_{NB} = 0.5, and λ_{EC} = 1. Two cases are studied: a first case with no uncertainty in T_e ($\delta_{T_e} = 0$), and a second case with uncertainty in T_e ($\delta_{T_e} \neq 0$). All simulations are made from t = 0.5 s to t = 2.5 s, i.e., for the ramp-up and early flat-top phases of the plasma discharge.

A. *Case 1:* $\delta_{T_e} = 0$

First, a feedforward simulation is run with the input signals corresponding to DIII-D shot 147634. A target $\bar{q}$ is created such that $\bar{q} = 1.1 q_{FF}$, where q_{FF} is the q-profile evolution obtained in feedforward. Then, a feedback simulation is run in which the controller attempts to drive q to the target $\bar{q}$ using the nominal control law. A value of k_N = 1.6 is taken.

Fig. 4 shows the time evolution of q at particular spatial locations, which correspond to the discretization nodes used for control, for both feedforward and feedback simulations together with the target $\bar{q}$. In Fig. 5, the q profile is showed at particular instants in time (t = 0.5 s, t = 1.25 s, and t = 2.5 s), also for feedforward and feedback simulations together with the target $\bar{q}$ profile. Fig. 6 shows the inputs

Preprint submitted to 2018 IEEE Conference on Control Technology and Applications. Received February 1, 2018.

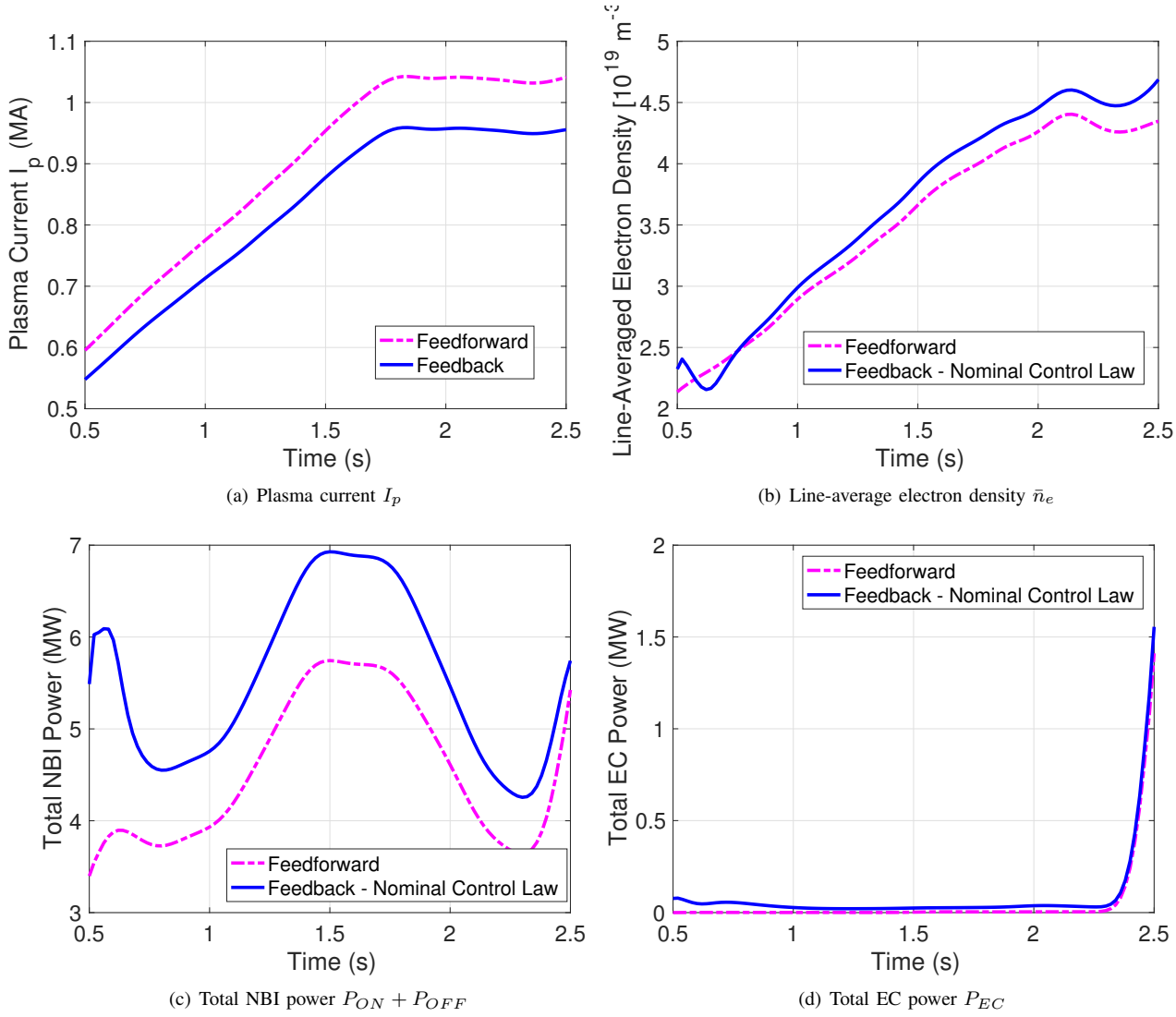

(a) Plasma current I_p

(b) Line-average electron density $\bar{n}_e$

(c) Total NBI power $P_{ON} + P_{OFF}$

(d) Total EC power P_{EC}

Fig. 6. Input signals for simulation case 1 ($\delta_{T_e} = 0$).

I_p, $\bar{n}_e$, $P_{ON} + P_{OFF}$, and P_{EC}, both in feedforward and feedback simulations. As it can be seen in Fig. 4 and Fig. 5, the nominal control law successfully drives q to its target $\bar{q}$ in all the different spatial locations. The q evolution converges to $\bar{q}$ faster as $\hat{\rho}$ increases, due most likely to the combined effect of boundary control (I_p control) with interior control (NBI & EC power, and $\bar{n}_e$ control). As showed in Fig. 6, the nominal controller uses a smaller I_p than in the feedforward case to achieve the target $\bar{q}$, whereas it uses a higher NBI and EC powers, and mostly a higher $\bar{n}_e$.

B. Case 2: $\delta_{T_e} \neq 0$

In this second part of the simulation study, an uncertainty δ_{T_e} is introduced which given by

$$\delta_{T_e}(\hat{\rho}, t) = -0.2T_e^{nom}(\hat{\rho}, t) - 0.25 \text{ keV}, \hat{\rho} \leq 0.3 \quad (29)$$

$$\delta_{T_e}(\hat{\rho}, t) = -0.2T_e^{nom}(\hat{\rho}, t) - 0.15 \text{ keV}, \hat{\rho} > 0.3, \quad (30)$$

i.e., an uncertainty composed by a time-varying, spatially-varying decrease of -20% T_e^{nom}, plus constant decreases of about -17% (at $\hat{\rho} \leq 0.3$) and -10% (at $\hat{\rho} > 0.3$) of the initial core-temperature experimental value.

The target $\bar{q}$ is taken in this case as $\bar{q} = q_{FF}$. First, a feedforward simulation is run with the input signals corresponding to DIII-D shot 147634. Second, a feedback simulation is run in which the controller attempts to drive q to $\bar{q}$ using the nominal control law. Finally, another feedback simulation is executed using the robust control law with the same objective of driving q to $\bar{q}$. The same value k_N = 1.6 is taken, so that the comparison between nominal and robust controllers is fair. Also, k_R = 0.1 is taken.

Fig. 7 shows the time evolution of q at particular spatial locations (again, the nodes used for control), Fig. 8 shows the q-profile at particular instants in time, and Fig. 9 shows the controlled inputs. All the figures show simulations for three different cases: feedforward, feedback under the nominal control law, and feedback under the robust control law. By comparing Fig. 7 with Fig. 4, it is possible to note how sensitive the prediction of the q profile is with respect to uncertainties in the electron temperature model. As it can be seen in Fig. 7 and Fig. 8, the robust control law successfully drives q to its target $\bar{q}$, whereas the nominal control law is unable to do so. It is interesting to see how the q evolution

Preprint submitted to 2018 IEEE Conference on Control Technology and Applications. Received February 1, 2018.

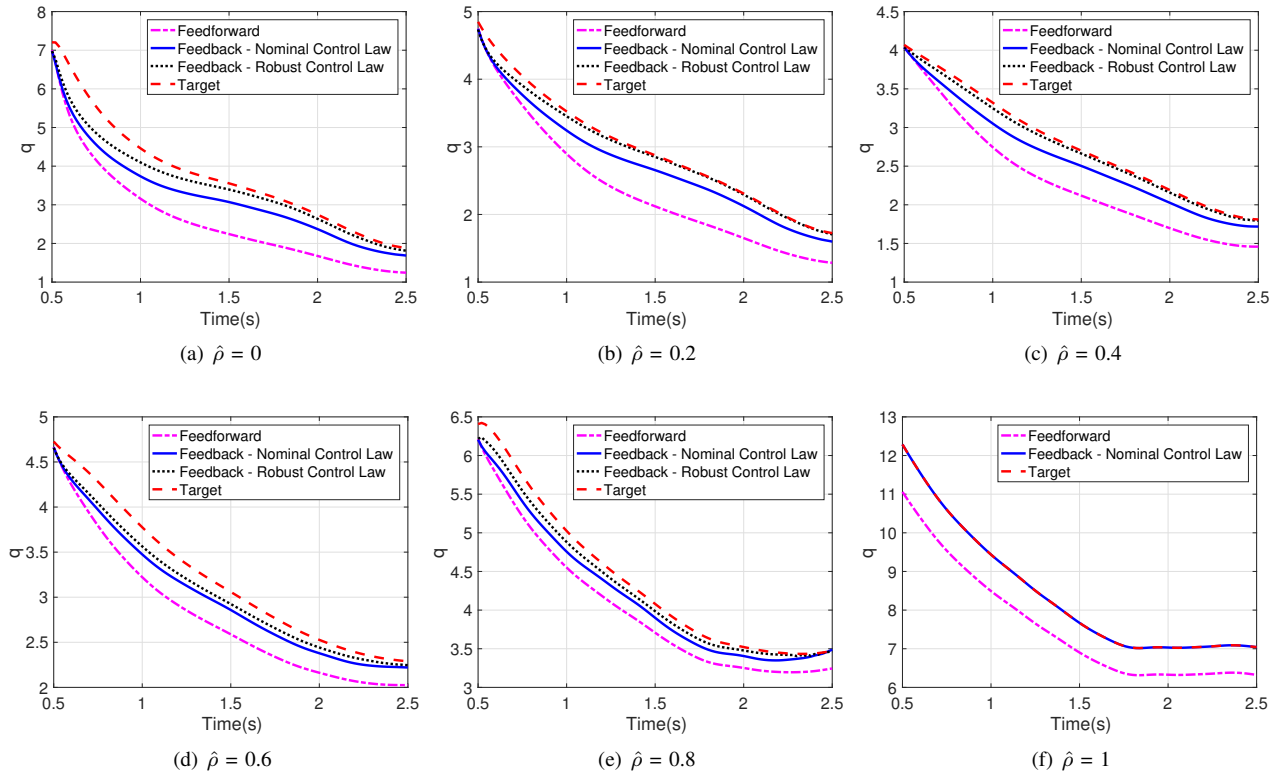

(a) $\hat{\rho} = 0$ (b) $\hat{\rho} = 0.2$ (c) $\hat{\rho} = 0.4$

(d) $\hat{\rho} = 0.6$ (e) $\hat{\rho} = 0.8$ (f) $\hat{\rho} = 1$

Fig. 7. Safety factor evolution at different locations for simulation case 2 ($\delta_{T_e} \neq 0$).

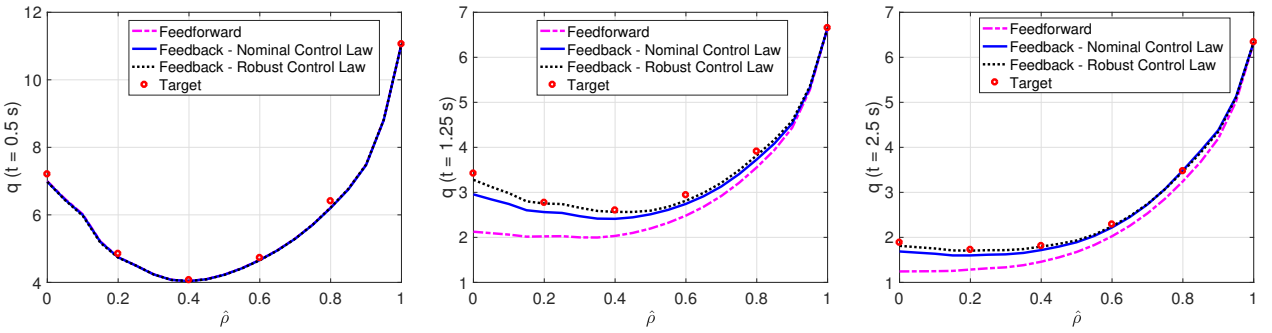

(a) $t = 0.50$ s (b) $t = 1.25$ s (c) $t = 2.50$ s

Fig. 8. Safety factor profiles for simulation case 2 ($\delta_{T_e} \neq 0$).

under robust-feedback converges to $\bar{q}$ faster as $\hat{\rho}$ decreases, i.e., the opposite to the case with no uncertainty under nominal-feedback. Again, this is most likely because of the major impact of the robust interior control in the plasma core. Fig. 6 shows that the controller uses the same I_p in feedforward and feedback, due to the fact that $\bar{q} = q_{FF}$. Both NBI and EC powers, together with $\bar{n}_e$, are higher when using robust-feedsback than when using nominal-feedback, except in the last ≈ 0.2 s of the simulation. It can also be seen that the nominal control law reaches saturation at the end of the simulation, but the q-profile evolution does not reach the target, showing a significantly more efficient control using the robust control law.

VI. Conclusions

A robust controller for q-profile regulation in tokamaks has been presented that makes use of feedback linearization and nonlinear damping techniques. It has been showed that the tokamak model employed in this work is always feedback linearizable, which is a powerful property that avoids approximate linearization of the system. Also, the use of feedback linearization allows for the ulterior use of nonlinear robust-control techniques. Nonlinear robust controllers are expected to have a better performance than linear robust controllers due to the highly nonlinear, uncertain nature of the plasma dynamics. Nonlinear damping techniques can be applied to this system because it is feedback linearizable. The controller has showed good performance in simulation for a DIII-D scenario, but it is applicable to any other tokamak scenario following an analog approach to the one showed in this paper.

References

[1] J. Wesson, *Tokamaks*. Oxford, UK: Clarendon Press, 1984.

Preprint submitted to 2018 IEEE Conference on Control Technology and Applications. Received February 1, 2018.

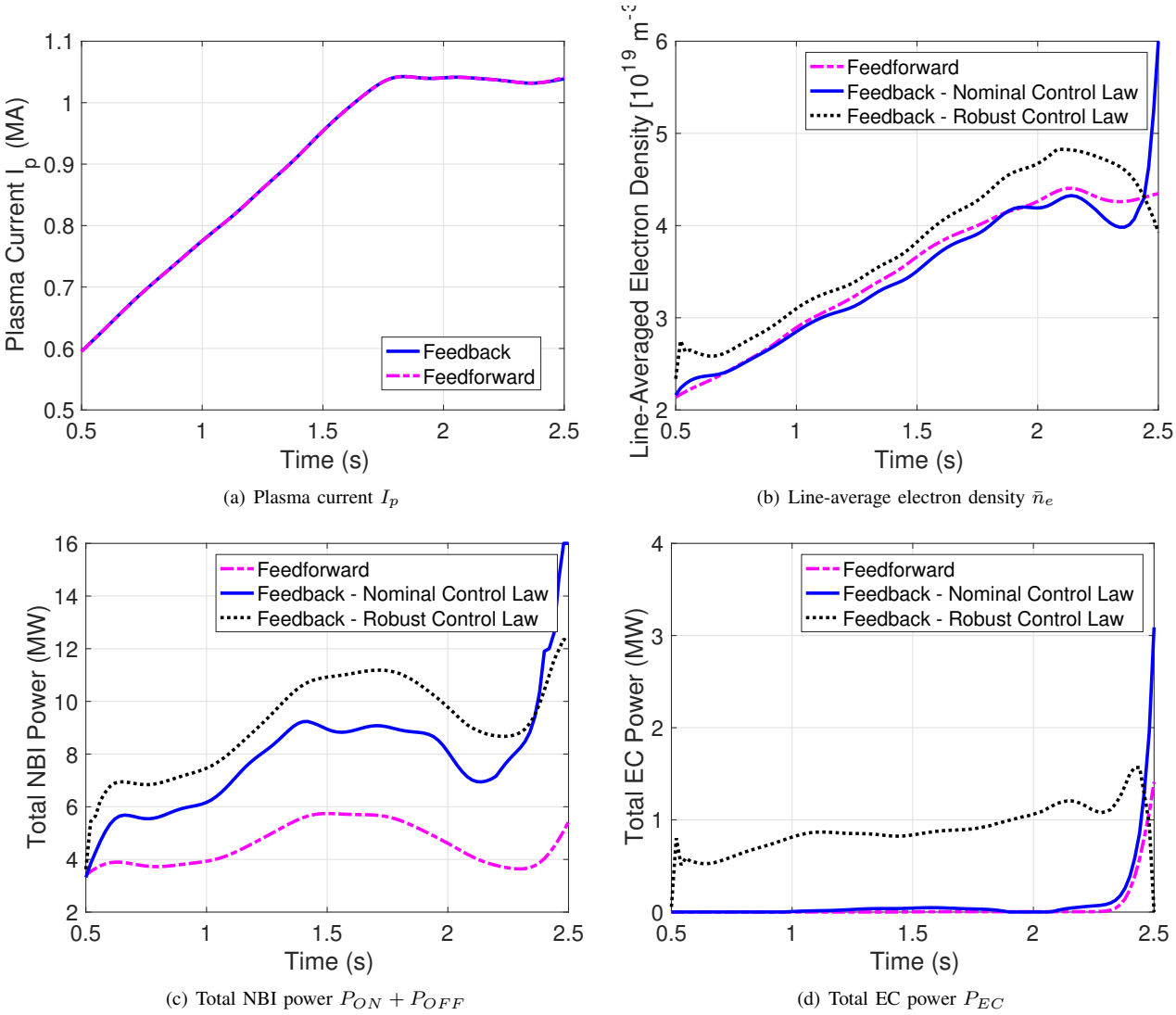

(a) Plasma current I_p

(b) Line-average electron density $\bar{n}_e$

(c) Total NBI power $P_{ON} + P_{OFF}$

(d) Total EC power P_{EC}

Fig. 9. Inputs signals for simulation case 2 ($\delta_{T_e} \neq 0$).

[2] J. Barton, M. Boyer, W. Shi, E. Schuster *et al.*, "Toroidal Current Profile Control During Low Confinement Mode Plasma Discharges in DIII-D via First-Principles-Driven Model-based Robust Control Synthesis," *Nuclear Fusion*, vol. 52, no. 123018, 2012.

[3] M. Boyer, J. Barton, E. Schuster *et al.*, "First-Principles-Driven Model-Based Current Profile Control for the DIII-D Tokamak via LQI Optimal Control," *Plasma Physics and Controlled Fusion*, vol. 55, no. 105007, 2013.

[4] M. Boyer, J. Barton, E. Schuster, M. Walker, T. Luce, J. Ferron, B. Penaflor, R. Johnson, and D. Humphreys, "Backstepping Control of the Toroidal Plasma Current Profile in the DIII-D Tokamak," *Control Systems Technology, IEEE Transactions on*, vol. 22, no. 5, pp. 1725–1739, Sept 2014.

[5] J. Barton, M. Boyer, E. Schuster *et al.*, "Physics-model-based nonlinear actuator trajectory optimization and safety factor profile feedback control for advanced scenario development in DIII-D," *Nucl. Fusion*, vol. 55, no. 093005, 2015.

[6] Z. Ilhan, W. Wehner, J. Barton, E. Schuster, D. Gates, S. Gerhardt, and J. Menard, "First-Principles-Driven Model-Based Optimal Control of the Current Profile in NSTX-U," in *Proceedings of the 2015 IEEE Multi-conference on Systems and Control*, 2015.

[7] D. Moreau *et al.*, "A two-time-scale dynamic model approach for magnetic and kinetic profile control in advanced tokamak scenarios on JET," *Nuclear Fusion*, vol. 48, 2008.

[8] F. Argomedo, C. Prieur, E. Witrant, and S. Bremond, "A Strict Control Lyapunov Function for a Diffusion Equation With Time-Varying Distributed Coefficients," in *IEEE Transactions on Automatic Control, 58, 2*, 2012.

[9] J. Barton, W. Wehner, E. Schuster, F. Felici, and O. Sauter, "Simultaneous Closed-loop Control of the Current Profile and the Electron Temperature Profile in the TCV Tokamak," *2015 IEEE American Control Conference*, 2015.

[10] J. Barton, K. Besseghir, J. Lister, and E. Schuster, "Physics-based control-oriented modeling and robust feedback control of the plasma safety factor profile and stored energy dynamics in ITER," *Plasma Physics and Controlled Fusion*, vol. 57, no. 115003, 2015.

[11] J. Barton, W. Shi *et al.*, "Physics-based Control-oriented Modeling of the Current Density Profile Dynamics in High-performance Tokamak Plasmas," *52nd IEEE International Conference on Decision and Control*, 2013.

[12] Y. Ou, C. Xu, and E. Schuster, "Robust Control Design for the Poloidal Magnetic Flux Profile Evolution in the Presence of Model Uncertainties," *IEEE Transactions on Plasma Science*, vol. 38, no. 3, pp. 375–382, 2010, http://ieeexplore.ieee.org/stamp/stamp.jsp?arnumber=05404914.

[13] A. Pajares and E. Schuster, "Safety Factor Profile Control in Tokamaks via Feedback Linearization," *55th IEEE Conference on Decision and Control*, 2016.

[14] F. Hinton and R. Hazeltine, "Theory of plasma transport in toroidal confinement systems," *Rev. Mod. Phys.*, vol. 48, pp. 239–308, 1976.

[15] Y. Ou, T. Luce, E. Schuster *et al.*, "Towards model-based current profile control at DIII-D," *Fusion Engineering and Design*, vol. 82, pp. 1153–1160, 2007.

[16] H. Khalil, *Nonlinear Systems*, 3rd ed. New Jersey: Prentice Hall, 2001.

[17] J. Nocedal and S. J. Wright, *Numerical Optimization*, 2nd ed. Springer, 2006.

Preprint submitted to 2018 IEEE Conference on Control Technology and Applications. Received February 1, 2018.